Design and Experimental Validation of High-Resolution Single-Shot Emittance Diagnostics for Heavy-Ion Beams

Garam Hahn, Tae-Keun Yang, Hyun Jong You, and Ji-Gwang Hwang

***Abstract*— A pepper-pot diagnostic device was developed to accurately and robustly retrieve particle distribution in horizontal and vertical phase spaces by single-shot emittance measurements. Two masks that differ in both composition and manufacturing method were fabricated: one made of phosphor bronze by an optical lithography process and another made of stainless steel (SUS) by laser cutting. Scanning electron microscope (SEM) measurements of the two masks revealed that the former is superior in terms of regularity and shape of the mask holes and is therefore more suitable to use. A new image-processing algorithm, namely, cluster noise removal method, was developed which improves the resolution of the phase-space distribution measurements over traditional methods. The device was tested in experiments with low-energy argon beams generated by an electron-cyclotron resonance (ECR) ion source at Korea Institute of Fusion Energy (KFE), Daejeon, South Korea. The results show that the diagnostics can robustly and reliably retrieve the four-dimensional (4-D) phase-space distribution of ion beams with a single-shot measurement.**

***Index Terms*— Background removal, four-dimensional (4-D) emittance, heavy-ion beams, low-energy beams, particle therapy, pepper-pot.**

I. Introduction

COMMISSIONING of a low-energy beam transport (LEBT) line is important [1] since the beam quality and intensity of the whole accelerator are mainly dominated by beam parameters such as Courant-Snyder parameters and emittances at the entrance of a linear accelerator. The LEBT line consists of an electron-cyclotron resonance (ECR) ion source to stably produce ion beams, a beam separator to discriminate target ion beams from unnecessary ion beams generated by background gas which is used to increase the possibility of collisions in plasma cells, and diagnostics to measure various beam parameters. A linear accelerator, which consists of radio frequency quadrupole (RFQ) and drift-tube linear (DTL) accelerators, is located downstream of the LEBT line and has a limited transverse acceptance determined by the physical aperture of a matching cell located at the beginning of the RFQ accelerator [2], [3].

With the conventional diagnostic methodologies [4] such as slit scanning and quadrupole scanning [5], commissioning of an LEBT line with the required beam quality is time-consuming and costly. In addition, these methods are not suitable for measuring horizontal-vertical coupling terms. ECR ion sources give rise to the coupling due to solenoidal and hexagonal magnetic fields, which are essential for trapping ion and electron beams inside a plasma chamber. There is an effort to complement the limit of the slit scanner using a rotatable stage, but the system requires a relatively longer space-about 83 cm [6]. This calls for a fast, robust, compact, and high-resolution beam diagnostics that can measure the coupling terms as well. The pepper-pot device has been devised [7], [8], experimentally demonstrated [9], [10] for electron and heavy-ion beams, and used for various applications [11]–[17] to achieve a high resolution and fast single-shot measurement by exploiting a micro-channel plate (MCP). These investigations, however, have not dealt with the manufacturing accuracy of the mask and sophisticated noise suppression generated by the MCP, which are crucial factors for achieving high resolution. Here, we have developed a pepper-pot diagnostic device including a reliable algorithm to achieve a high resolution. It enables a single-shot measurement with an accurate reconstruction of beam distribution in four-dimensional (4-D) phase space at a low beam current since it includes an MCP which is able to amplify the signal by four orders of magnitude. This compact instrument accurately measures the beam emittance and Courant-Snyder parameters simultaneously in horizontal and vertical directions for low-energy beams.

Manuscript received March 5, 2021; revised July 21, 2021; accepted August 7, 2021. Date of publication August 19, 2021; date of current version September 10, 2021. This work was supported by the National Cancer Center Research Grant 2110380-1 (Study of Beam Scanning Nozzle and Dosimetry Method for the Next Generation Flash Particle Therapy). The Associate Editor coordinating the review process was Dr. Branislav Djokic. *(Corresponding authors: Garam Hahn; Ji-Gwang Hwang.)*

Garam Hahn is with Pohang Accelerator Laboratory, Pohang University of Science and Technology (POSTECH), Pohang 37673, Republic of Korea (e-mail: garam@postech.ac.kr).

Tae-Keun Yang is with Korea Institute of Radiological and Medical Sciences, Seoul 01812, Republic of Korea.

Hyun Jong You is with Korea Institute of Fusion Energy, Daejeon 34133, Republic of Korea.

Ji-Gwang Hwang is with the Institute for Accelerator Physics, Helmholtz-Zentrum Berlin, 12489 Berlin, Germany (e-mail: ji-gwang.hwang@helmholtz-berlin.de).

Digital Object Identifier 10.1109/TIM.2021.3106129

II. Physical Design and Mask Fabrication

The pepper-pot diagnostic device consists of a metallic mask with a pinhole array for deconvolutioning the position and angular information of charged-particle beams by a small spatial opening, an MCP for amplifying signal intensity by a factor of 10^4, a phosphor screen for converting

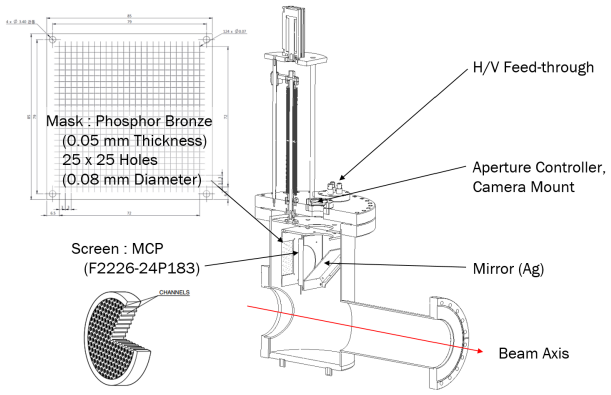

Fig. 1. Technical drawing of pepper-pot emittance device which consists of metallic mask, MCP, phosphor screen, and mirror.

electrons to visible light, and optics for measuring the profile. Since the beam intensity on the phosphor screen is significantly reduced by the small opening of the mask, the MCP is required to improve the signal-to-noise ratio of the detector. A technical drawing of the pepper-pot device is shown in Fig. 1.

A. Physical Design

The fundamental principle of the pepper-pot emittance device is the reconstruction of position and angular distribution of incident beams as in a slit-scan method but in a single shot by applying a metallic mask which has equidistant pinholes with the same diameter. When the incident beams are split into beamlets by the pinholes on the mask, each beamlet creates a spot on the phosphor screen located downstream of the mask. This allows for the deconvolution of the angular distribution of the beam based on the predefined distance between the mask and the screen. The resolution limit of emittance measurements using the pepper-pot device is fundamentally determined by the ratio of the distance between the mask and the MCP to the pinhole diameter and the precision and deviation of the diameter of pinholes [18]. Assuming a Gaussian distribution of incident particles and no $x-y$ coupling, the measurement resolution of the unnormalized emittance using the pepper-pot device can be expressed as

$$\Delta\epsilon_{x,y} = \frac{2\Delta\sigma}{d}\sqrt{\left(\frac{a}{\sqrt{12}}\frac{\beta_{x,y}}{1+\alpha_{x,y}^2}\right)^2 + \left(\epsilon_{x,y}d\right)^2} \qquad (1)$$

where $\Delta\sigma$ is the resolution of the imaging system, d is the distance between the mask and the MCP, a is the hole diameter, $\alpha_{x,y}$ and $\beta_{x,y}$ are the Courant-Snyder parameters, and $\epsilon_{x,y}$ is the unnormalized transverse emittance. In the square root of (1), the first term is always greater than the second term for $a\beta \gg \epsilon_{x,y}d$. Therefore, the resolution of the emittance measurement can be approximated by $\epsilon_{x,y} \sim (a\beta\Delta\sigma)/d$. In addition, the larger $\alpha_{x,y}$ value which interprets the derivative of the β-function yields further improvement of the resolution. To determine the optimal set of parameters, the distance between the mask and the MCP and the hole diameter were varied with the beam parameters of the LEBT of the KHIMA accelerator [19]–[21] that has a kinetic energy of 8 keV/u,

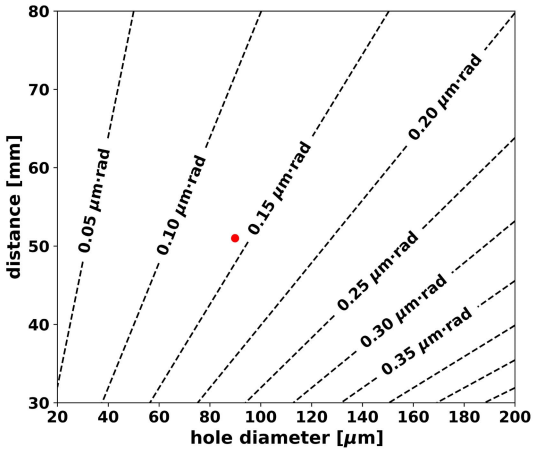

Fig. 2. Systematic resolution of pepper-pot device as functions of pinhole diameter and distance between the mask and the MCP with the beam energy of 8 keV/u, the unnormalized emittance of 36 mm · mrad (normalized emittance of 0.15 mm · mrad), and $\alpha_{x,y} = 0$ which corresponds to the worst case from (1). All values are unnormalized emittances and the red dot represents our design parameters.

TABLE I
MAIN SPECIFICATIONS OF THE DESIGNED PEPPER-POT DEVICE

Name	Value	Unit
Dimension of mask hole-array	75 × 75	mm
Mask hole configuration	25 × 25-1	–
Mask hole-to-hole distance	3.0	mm
Mask hole diameter	89.9 ± 1.3	μm
Mask to MCP distance	51	mm
MCP active radius	37.5	mm

a unnormalized emittance of 36 mm · mrad (a normalized emittance of 0.15 mm · mrad), and a beam size of 10 mm. The calculation was performed within reasonable boundaries, and the result is shown in Fig. 2.

When the second term in the square root of (1) is larger than the contribution by the hole diameter, the resolution is not dramatically improved by reducing the hole diameter, whereas the intensity depends quadratically on the diameter. The intensity increment, however, would reduce the statistical error on emittance determination. A greater distance between the mask and the screen can easily improve the resolution of the measurement. However, it not only reduces the number of data points for the phase-space reconstruction by increasing the distance between the holes but also occupies much space, which is not suitable for low-energy beamlines. With the hole diameter of 90 μm that is determined by technical limitations (see Section II-B), the distance between the mask and the screen was optimized to be 51 mm to achieve a resolution of 0.15 mm · mrad. The measurement resolution of the unnormalized emittance is therefore 0.15 mm · mrad which corresponds to 0.4% of the emittance value in the LEBT line. With these optimal parameters, the distance between the holes is determined to be 3 mm since the beam spot size on the MCP defined by the beam angle and the mask to MCP distance ($\sigma_{x',y'} \times d$) is below 0.5 mm with a moderate $\alpha_{x,y}$ value which is required for improving the resolution further. The main design parameters are listed in Table I.

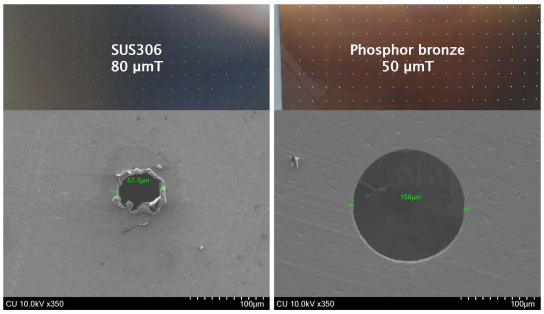

Fig. 3. Picture of SEM measurements of two masks, stainless steel (SUS 306) with a thickness of 80 μm fabricated by the laser-cutting technique and phosphor bronze with a thickness of 50 μm fabricated by lithography.

B. Precise Mask Fabrication for High-Resolution Pepper-Pot Device

The manufacturing accuracy and reproducibility of the pepper-pot mask are crucial to achieving the high resolution of the detector. Two types of masks were fabricated by substantially different manufacturing techniques. Two masks that differ in both composition and manufacturing method were fabricated: one made of phosphor bronze by an optical lithography process and another made of stainless steel (SUS) by laser cutting. The distinct fabrication processes necessitated the choice of different materials. The thicknesses of the masks were determined to be 50 μm for the phosphor bronze and 80 μm for SUS to suppress the secondary electrons. A hole diameter of 60 μm is typically achievable by laser cutting with accurate positioning. Local heat deposition, however, can distort the shape of the hole. Since hole distortion leads to the change in the image shape when the hole diameter is close to the image size, the manufacturing tolerance of hole diameters, hole shape, and distance of both masks were investigated by scanning electron microscope (SEM) measurements. The SEM images of the two masks are shown in Fig. 3.

Irregular burrs formed by localized heat were observed in the SEM measurement of the SUS mask. The hole size becomes noticeably inhomogeneous; this inhomogeneity necessarily increases the error in the measured emittance due to uncertain beam widths. On the other hand, the phosphor bronze mask has about 67% bigger hole diameter compared with the designed value. This would deteriorate the resolution by more than 60% as shown in Fig. 2. Finally, we successfully acquired ahole size comparable to our design value by controlling the processing time for the etching solution. The mask with a hole diameter of 90 μm and an inter-hole spacing of 3 mm reduces the beam current by a factor of 1429. This does call for the MCP to amplify the signal intensity at the screen. The diameter of randomly sampled holes was measured and this is normally distributed with a mean of 89.9 μm and a standard deviation of 1.3 μm. The result of the SEM measurement of the final mask is shown in Fig. 4.

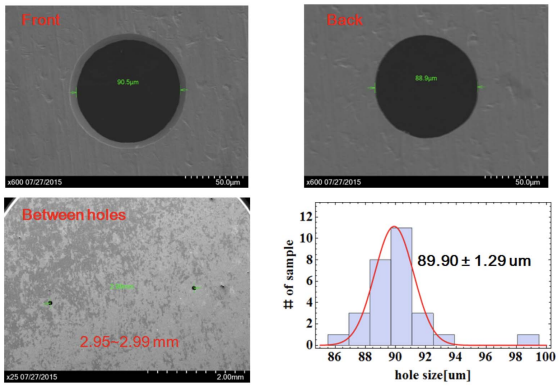

Fig. 4. SEM measurement results for the final phosphor-bronze mask after optimization of the fabrication process. The holes have a diameter of 89.9 ± 1.29 μm.

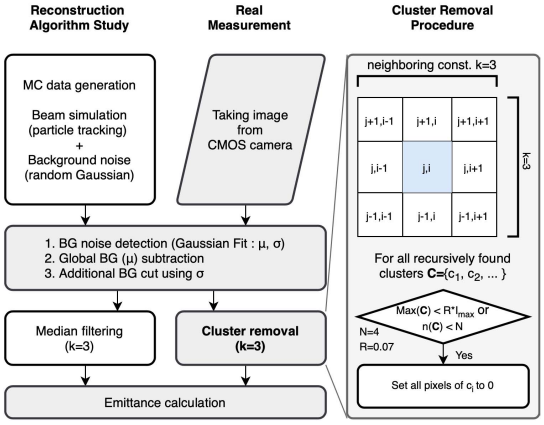

Fig. 5. Flowchart of the image processing algorithm for background noise reduction.

III. Image Processing and Noise Filtering

The image of the pepper-pot device generated by an MCP and phosphor screen contains not only signals created by charged beams but also background noise which stems from the dark current of the CMOS sensor, blur characteristics of the phosphor screen, secondary particles scattered at the mask, and ambient light partially reflected by metallic surfaces of the surrounding structures. Several previous image processing studies were performed without proper background noise rejection [22]–[25]. The noise that is not cleanly removed causes inaccurate results of the phase-space distribution of the beam as it is considered as the beam signal during the reconstruction stage. Furthermore, imprecise discrimination of the background noise by a constant leveling leads to misinterpretation of beam spot sizes, resulting in intolerable stochastic error for low-emittance beams. We propose a robust algorithm to suppress the influence of the background noise in the pepper-pot image analysis as elaborated in Fig. 5.

The newly developed algorithm features two characteristics: 1) a pre-verification procedure that is accomplished with an artificial image generated by a particle tracking simulation [26] based on the Monte Carlo (MC) method and 2) an advanced background removal method (cluster-removal filter) for effectively suppressing speckle and stray noises. This technique enables precise subtraction of the background noise and the investigation of the characteristics of different filters.

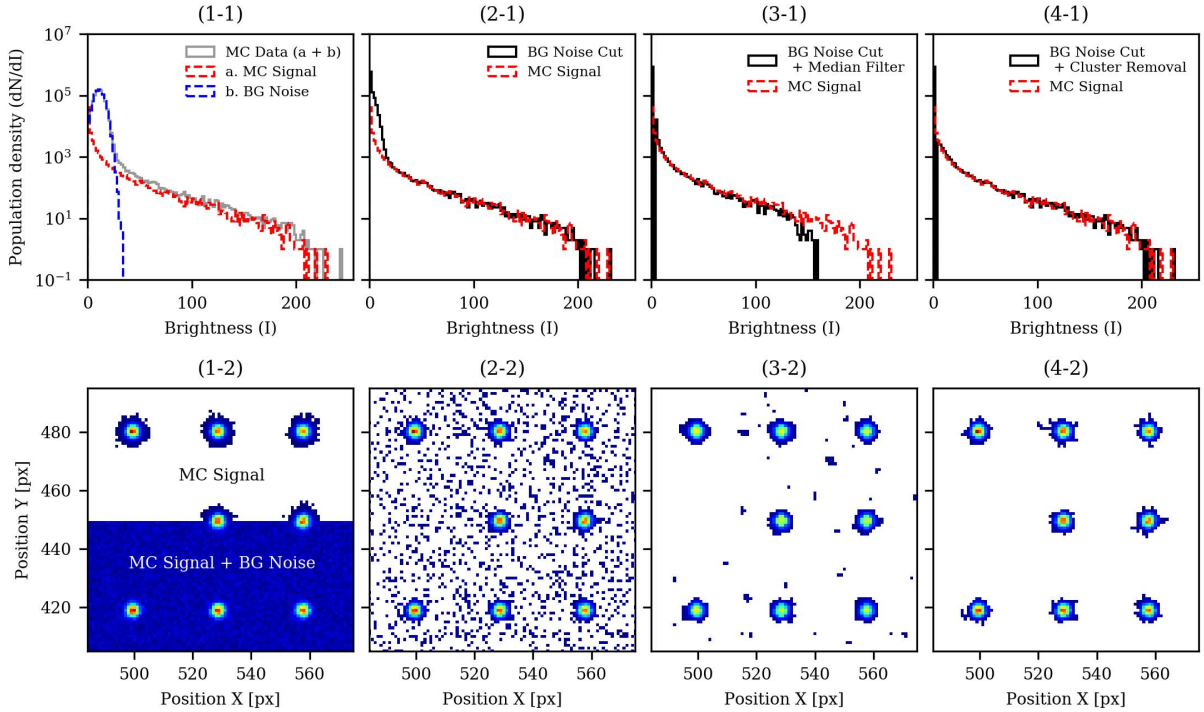

Fig. 6. Intensity histograms (upper side) and images (lower side) for: 1) unprocessed; 2) thresholding technique; 3) median filter; and 4) cluster-removal image processing. Red lines represent the intensity distribution of the original image generated by a particle tracking simulation and black lines are the intensity distribution after applying the filters.

The detailed procedure for generating the artificial image is as follows.

1) A Gaussian beam distribution on a virtual plane at the entrance of the pepper-pot mask was generated until the number of particles that pass through the mask holes is up to a certain value for the creation of an artificial image using the Courant-Snyder parameters (α_x, β_x, α_y and β_y) and RMS emittances (ϵ_x and ϵ_y) [27]. The number of generated particle for each pepper-pot hole is defined as

$$n\left(\vec{X}_{i,j}\right) = \left\lfloor Ae^{-\frac{(x-x_j)^2}{2\epsilon_x\beta_x}} e^{-\frac{(y-y_j)^2}{2\epsilon_y\beta_y}} \right\rfloor \tag{2}$$

where $\vec{X}_{i,j} = (x_i, y_j)$ and A is an arbitrary number that controls the total number of generated particles. Vertical and horizontal angular distributions (x_i', y_j') for each pepper-pot hole can be expressed as

$$x_i', y_j' = G_r\left(-\frac{\alpha_x}{\beta_x}x_i, \sqrt{\frac{\epsilon_x}{\beta_x}}\right), \quad G_r\left(-\frac{\alpha_y}{\beta_y}y_j, \sqrt{\frac{\epsilon_y}{\beta_y}}\right) \tag{3}$$

where G_r is a Gaussian random number generation function defined as $G_r(\mu, \sigma)$, where μ is the mean value and σ is the standard deviation.

2) Generated particles were tracked to the MCP surface based on the initial angle and the position of each particle. The 2-D histogram of the particle distribution, named the MC signal distribution, is calculated with a bin size that is similar to the resolution of the camera.

3) A simple Gaussian white noise $G_r(l_n, d_n)$ was added uniformly to the MC signal distribution as the background noise, where l_n is the mean noise level and d_n is the noise deviation level of the pixels.

4) The intensity of all pixels is collectively adjusted to be less than the bit depth of the camera.

Fig. 6 (1-1) and (1-2) shows an example of the intensity histogram and the artificial image, generated by the procedure described above. With the artificial image, which is qualitatively consistent with real images obtained by beam experiments, we performed two steps of image processing to disentangle the background noise. The background noise, which looks a dark white noise, typically makes the highest peak in the brightness space. In the first step, the noise peak is detected using a Gaussian fit and the fit mean value is globally subtracted from all pixels. An additional background cut is performed in which the noise elements below a certain brightness threshold are set to zero. The threshold is determined as a function of the standard deviation from the said Gaussian fit. The population density of the pixel intensity indicates that the residual background noise remains partial at the low-intensity region [see Fig. 6 (2-1)].

As the second step, we tested the performance of filtering techniques for 2-D datasets such as median filter and cluster-removal filter. The median filter is well-known for reducing a randomly scattered impulse noise which is caused by dead pixels and a Gaussian noise by the MCP [28], [29]. The cluster-removal filter, newly developed in this study, rejects multi-dimensionally clustered noises without distortion of the beam signals which were characterized by continuous distribution with a higher intensity peak in the middle [see Fig. 6 (1-1)]. The developed filter discerns clusters by scanning recursively over adjacent $k^2 - 1$ pixels, and then removes the clusters unless they fulfill the pre-defined criteria: 1) the maximum value of the cluster must be larger than a value that proportionals to the brightest level in the image

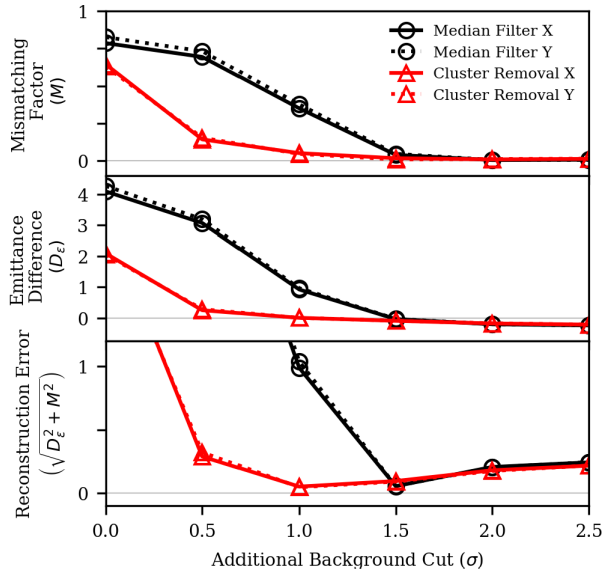

Fig. 7. Performance comparison of two algorithms according to the variation in the additional background cut.

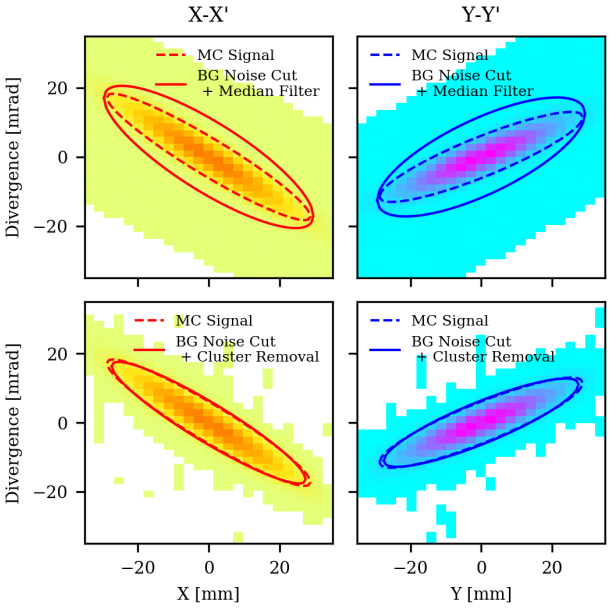

Fig. 8. Reconstructed phase space comparison of two algorithms when their additional background cuts are 1-σ.

(7% was used here) and 2) the number of pixels of the cluster must be larger than a number N ($N = 4$ was used here). The algorithm effectively eliminates relatively low-intensity noise while not invading beam signals since filtering affects only the low-intensity pixels. In contrast, the median filter with a minimum kernel size of $k = 3$ dilutes beam signals, although this does remove the residual background noise since it replaces each entry with the median of neighboring entries as shown in Fig. 6 (3-1 and 3-2).

To evaluate the reconstruction accuracy of both methods quantitatively, we calculated the mismatching factor and emittance difference. The mismatching factor indicates the difference between two ellipses in $x - x'$ or $y - y'$ phase space using the Courant-Snyder parameters and the emittance difference is the deviation of the measured value from the real-beam emittance. The results are shown in Fig. 7.

The mismatching factor [30] and the emittance difference are defined as

$$M = \sqrt{\left(R + \sqrt{R^2 - 4}\right)/2} - 1 \tag{4}$$

$$D_\epsilon = (\epsilon_r - \epsilon_m)/\epsilon_m \tag{5}$$

where $R = \beta_r\gamma_m + \beta_m\gamma_r - 2\alpha_m\alpha_r$, β, γ, and α are the Courant-Snyder parameters, ϵ represents the RMS emittance, and subscripts r and m denote the reconstructed and MC generated values, respectively. The mismatching factor quantifies the difference between two ellipses as a value between 0 and 1. Both factors indicate that the measured value is close to the beam parameters when it vanishes. To simultaneously minimize two independent factors, the quantity $(D^2 + M^2)^{1/2}$ was defined as the reconstruction error index. As shown in Figs. 7 and 8, compared with the median filtering technique, the cluster-removal method with $k = 3$ is insensitive to the additional background cut and has lower reconstruction error. Therefore, the cluster removal algorithm with an additional background cut of 1.0–1.5 as a background removal image processing algorithm is implemented to the developed pepper-pot device. The phase-space reconstruction code also includes the correction of rotation and translation based on multi-dimensional matrices to mitigate the relative angular misalignment errors between the MCP, the mirror, and the CMOS camera with respect to the mask.

IV. Beam Experiment and 4-D Emittance Calculation

We treat the beam dynamics of charged particles in accelerators using 6-D phase-space coordinates. In many cases, it can be simplified to 2-D $x-x'$, $y-y'$, and $z-\delta_E$ sub-phase spaces when all beam manipulation objects consist of linear components such as quadrupole and dipole magnets without misalignments. However, inter-plane correlations can be produced by non-linear fields such as fringe field of magnets, sextupoles, solenoids, and a misalignment of magnets and radio frequency instruments and it can lead to the coupling of beam dynamics between two transverse phase spaces [31], [32]. Particularly, solenoids are commonly used in an ion source to trap plasma and in a LEBT to focus the beams effectively, but they make helical beam motions which transfer the particle's momentum of one axis to the other. Inter-plane coupled physical quantities are generated, transferred, and changed every time when the beam passes such non-linear fields. Such phenomena could be erroneously regarded as unexpected emittance changes if one uses the conventional slit-scan emittance meter that measures only 2-D phase spaces. However, quantifying the amount of inter-plane coupling has been accessible using pepper-pot diagnostic device, since it can measure the full 4-D beam distribution with a single-shot scan. Furthermore, quantitative controlling or minimizing the inter-plane coupled physical quantities is also possible using the pepper-pot emittance meter together with skew quadrupoles.

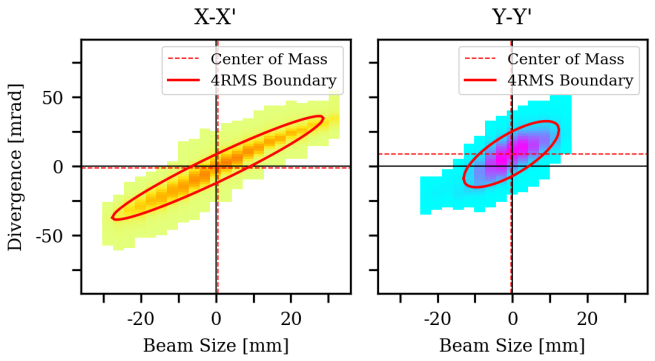

Fig. 9. Measured $x - x'$ and $y - y'$ phase-space distribution.

The 4-D beam matrix C can be expressed by the 4×4 symmetric second moments as

$$C = \begin{bmatrix} \langle xx \rangle & \langle xx' \rangle & \langle xy \rangle & \langle xy' \rangle \\ \langle x'x \rangle & \langle x'x' \rangle & \langle x'y \rangle & \langle x'y' \rangle \\ \langle yx \rangle & \langle yx' \rangle & \langle yy \rangle & \langle yy' \rangle \\ \langle y'x \rangle & \langle y'x' \rangle & \langle y'y \rangle & \langle y'y' \rangle \end{bmatrix}. \tag{6}$$

The beam matrix contains ten unique elements, four of which describe the coupling. When there exists a coupling between the horizontal and vertical planes, at least one of the elements of the off-diagonal submatrix is non-zero. The 4-D RMS emittance is the square root of the determinant of the beam matrix C, and the projected beam rms emittances ϵ_x and ϵ_y are the square roots of the determinants of the on-diagonal 2×2 sub-matrices [33]. The intensity distribution $W_{i,j}(x', y')$ of the beamlets which correspond to each pepper-pot hole of the mask (x_i, y_j) can be measured in the experiment, and the result can be translated to the moments $\langle \mu\nu \rangle$ by

$$\langle \mu\nu \rangle = \frac{\sum_i \sum_j \iint W_{i,j}(x', y') \mu\nu dx'dy'}{\sum_i \sum_j \iint W_{i,j}(x', y') dx'dy'} \tag{7}$$

where i and j indicate the numbers of row and column of the beamlet array, respectively, and μ and ν can be replaced by x, x', y, or y' variables. The variables x, x', y, or y' must be defined with respect to the beam center of mass before the calculation of the moments.

Beam experiments were performed using ion beams generated by an 18-GHz superconducting ECR ion source at Korea Institute of Fusion Energy (KFE), Daejeon, South Korea. This ion source is designed to extract a wide range of ion elements from gas to metal, and the maximum output current is optimized especially for the extraction of Ar^{16+} [34], [35]. The pepper-pot device is installed in the downstream of the ion source. In our measurement, Ar^{8+} ion beam was used with a current of 70 μA and the beam is extracted from the plasma cell of the ion source with a voltage of 24 kV. The phase ellipses in the horizontal and vertical directions are measured using the developed pepper-pot device.

As shown in Fig. 9, the unnormalized RMS horizontal and vertical beam emittances are measured to be 71.87π and 49.21π mm $\cdot$ mrad, respectively, when the adaptive baseline cut and an additional background cut of 1.5 were applied. The beam diverges in both the directions. As expressed in (7), the numerator is the same constant for all the components so that the emittance given by a determinant of the beam matrix is independent of linear intensity scaling. Using (6) and (7), the beam matrix is calculated as follows:

$$C_{\text{measured}} = \begin{bmatrix} 181.41 & 231.83 & 31.55 & 13.51 \\ 231.83 & 324.85 & 44.63 & 24.00 \\ 31.55 & 44.63 & 36.48 & 50.37 \\ 13.51 & 24.00 & 50.37 & 135.30 \end{bmatrix}. \tag{8}$$

The beam matrix has non-zero values in the off-diagonal submatrices indicating coupling between the transverse dimensions through solenoids and hexapoles inside ECRIS and a focusing solenoid and analyzing dipole outside ECRIS. We observed that the light produced by the MCP is reflected partially by surroundings such as the mirror, the mask, and vacuum chamber and then causes strong background noise on the measured image. It is challenging to predict the emittance precisely when the background light dilutes the picture of the holes. A vacuum-compatible coating technology is considered for further upgrade of the device.

V. Conclusion

A robust and reliable pepper-pot diagnostic device has been analytically and numerically illustrated that enables a fast single-shot emittance measurement in 4-D phase spaces for heavy-ion beams. The resolution of the device depends on the manufacturing quality of the mask and its mechanical structure. The structure of the device was carefully optimized and the fabrication quality of the mask has been proven through SEM measurement. In addition, a new algorithm is developed for rejecting background noise which strongly dilutes the resolution and accuracy of the retrieval of the phase-space distribution of the device. The algorithm is robust to the variation in the additional background cut, which can be introduced when the threshold in the initial treatment adopts an inappropriate evaluation. The pepper-pot device was validated experimentally using Ar^{8+} ion beams with a current of 70 μA and kinetic energy of 4.8 keV/u produced by an 18-GHz superconducting ECR ion source at KFE. The result shows reliable measurements of unnormalized RMS horizontal and vertical beam emittances, which were measured to be 71.87π and 49.21π mm $\cdot$ mrad, respectively.

Acknowledgment

The authors acknowledge the development of ultra-high vacuum-compatible instrumentation by Bo-Sung Kim at ITS Vac., Daejeon, South Korea.

References

[1] D. Ratschko, B. G. Zhou, D. Knolle, and M. Glaser, "Investigations on ion beams from a high-current ion source," *IEEE Trans. Instrum. Meas.*, vol. 46, no. 2, pp. 588–591, Apr. 1997.

[2] E.-S. Kim, J. Bahng, J.-G. Hwang, B.-H. Choi, H.-J. Kim, and D.-O. Jeon, "Start-to-end simulations for beam dynamics in the RISP heavy-ion accelerator," *Nucl. Instrum. Methods Phys. Res. A, Accel. Spectrom. Detect. Assoc. Equip.*, vol. 794, pp. 215–223, Sep. 2015.

[3] Y. Lee, E.-S. Kim, Z. Li, and G. Hahn, "IH-DTL design with KONUS beam dynamics for KHIMA project," *Nucl. Instrum. Methods Phys. Res. A, Accel. Spectrom. Detect. Assoc. Equip.*, vol. 801, pp. 51–57, Nov. 2015.

[4] D. J. Clark, "Invited paper beam diagnostics and instrumentation," *IEEE Trans. Nucl. Sci.*, vol. NS-13, no. 4, pp. 15–23, Aug. 1966.

[5] J.-G. Hwang *et al.*, "Analysis on effects of transverse electric field in an injector cavity of compact-ERL at KEK," *Nucl. Instrum. Methods Phys. Res. A, Accel. Spectrom. Detect. Assoc. Equip.*, vol. 753, pp. 97–104, Jul. 2014.

[6] C. Xiao, X. N. Du, L. Groening, and M. Maier, "Refining the evaluation of eigen emittances measured by the dedicated four-dimensional emittance scanner ROSE," *Nucl. Instrum. Methods Phys. Res. A, Accel. Spectrom. Detect. Assoc. Equip.*, vol. 964, Jun. 2020, Art. no. 163828.

[7] L. E. Collins and P. T. Stroud, "Extraction of high current ion beams with low divergence," *Nucl. Instrum. Methods*, vol. 26, pp. 157–166, Feb. 1964.

[8] A. Van Steenbergen, "Evaluation of particle beam phase space measurement techniques," *Nucl. Instrum. Methods*, vol. 51, no. 2, pp. 245–253, May 1967.

[9] Y. Yamazaki, T. Kurihara, H. Kobayashi, I. Sato, and A. Asami, "High-precision pepper-pot technique for a low-emittance electron beam," *Nucl. Instrum. Methods Phys. Res. A, Accel. Spectrom. Detect. Assoc. Equip.*, vol. 322, no. 2, pp. 139–145, Nov. 1992.

[10] T. Hoffmann, W. Barth, P. Forck, A. Peters, P. Strehl, and D. Liakin, "Emittance measurements of high current heavy ion beams using a single shot pepperpot system," *AIP Conf.*, vol. 546, no. 1, pp. 432–439, 2000.

[11] S. Fritzler *et al.*, "Emittance measurements of a laser-wakefield-accelerated electron beam," *Phys. Rev. Lett.*, vol. 92, no. 16, Apr. 2004, Art. no. 165006.

[12] S. Jolly *et al.*, "Data acquisition and error analysis for pepperpot emittance measurements," in *Proc. DIPAC Conf.*, 2009, pp. 1–3.

[13] S. Kondrashev, A. Barcikowski, B. Mustapha, P. N. Ostroumov, and N. Vinogradov, "Development of a pepper pot emittance probe and its application for ECR ion beam studies," *Nucl. Instrum. Methods Phys. Res. A, Accel. Spectrom. Detect. Assoc. Equip.*, vol. 606, no. 3, pp. 296–304, Jul. 2009.

[14] C. M. S. Sears, A. Buck, K. Schmid, J. Mikhailova, F. Krausz, and L. Veisz, "Emittance and divergence of laser wakefield accelerated electrons," *Phys. Rev. Special Topics-Accel. Beams*, vol. 13, no. 9, Sep. 2010, Art. no. 092803.

[15] E. Brunetti *et al.*, "Low emittance, high brilliance relativistic electron beams from a laser-plasma accelerator," *Phys. Rev. Lett.*, vol. 105, no. 21, Nov. 2010, Art. no. 215007.

[16] G. G. Manahan *et al.*, "Characterization of laser-driven single and double electron bunches with a permanent magnet quadrupole triplet and pepper-pot mask," *New J. Phys.*, vol. 16, no. 10, Oct. 2014, Art. no. 103006.

[17] T. Yorita *et al.*, "Developments of fast emittance monitors for ion sources at RCNP," *Rev. Sci. Instrum.*, vol. 87, no. 2, 2016, Art. no. 02B928.

[18] J. G. Wang, D. X. Wang, and M. Reiser, "Beam emittance measurement by the pepper-pot method," *Nucl. Instrum. Methods Phys. Res. A, Accel. Spectrom. Detect. Assoc. Equip.*, vol. 307, nos. 2–3, pp. 190–194, Oct. 1991.

[19] T.-K. Yang *et al.*, "Status of beam diagnostics at KHIMA facility," in *Proc. IBIC*, 2015, pp. 126–130.

[20] H. Yim, C. Park, C. Kim, W. Hwang, G. Hahn, and J. Hwang, "Korea heavy-ion medical accelerator project," in *Proc. 7th Int. Part. Accel. Conf. (IPAC)*, Busan, South Korea, May 2016, pp. 4243–4247.

[21] Y. Lee, E.-S. Kim, C. Kim, J. Bahng, Z. Li, and G. Hahn, "Start-to-end simulations for beam dynamics in the injector system of the KHIMA heavy ion accelerator," *Nucl. Instrum. Methods Phys. Res. A, Accel. Spectrom. Detect. Assoc. Equip.*, vol. 861, pp. 7–15, Jul. 2017.

[22] S. K. Guharay, K. Tsumori, M. Hamabe, Y. Takeiri, O. Kaneko, and T. Kuroda, "Simple emittance measurement of H-beams for neutral beam injectors in magnetic fusion," *Rev. Sci. Instrum.*, vol. 67, no. 7, pp. 2534–2537, Jul. 1996.

[23] H. R. Kremers, J. P. M. Beijers, and S. Brandenburg, "A pepper-pot emittance meter for low-energy heavy-ion beams," *Rev. Sci. Instrum.*, vol. 84, no. 2, Feb. 2013, Art. no. 025117.

[24] J. Pitters *et al.*, "Pepperpot emittance measurements of ion beams from an electron beam ion source," *Nucl. Instrum. Methods Phys. Res. A, Accel. Spectrom. Detect. Assoc. Equip.*, vol. 922, pp. 28–35, Apr. 2019.

[25] Y. Morita *et al.*, "Developments of real-time emittance monitors," *Rev. Sci. Instrum.*, vol. 91, no. 4, Apr. 2020, Art. no. 043303.

[26] O. Apsimon, B. Williamson, and G. Xia, "A numerical approach to designing a versatile pepper-pot mask for emittance measurement," *Nucl. Instrum. Methods Phys. Res. A, Accel. Spectrom. Detect. Assoc. Equip.*, vol. 943, Nov. 2019, Art. no. 162485.

[27] G. Hahn, "Design of energy selection system for cyclotron based carbon therapy facility," Ph.D. dissertation, Dept. Phys., Univ. Seoul, Seoul, South Korea, Jul. 2017.

[28] J.-Y. Chang and J.-L. Chen, "Classifier-augmented median filters for image restoration," *IEEE Trans. Instrum. Meas.*, vol. 53, no. 2, pp. 351–356, Apr. 2004.

[29] I. Andreadis and G. Louverdis, "Real-time adaptive image impulse noise suppression," *IEEE Trans. Instrum. Meas.*, vol. 53, no. 3, pp. 798–806, Jun. 2004.

[30] K. Crandall and D. Rusthoi, "Trace 3-D documentation," Inst. Published, Stanford Linear Accel. Center, Menlo Park, CA, USA, Tech. Rep. 886, 1997.

[31] D. H. Dowell, F. Zhou, and J. Schmerge, "Exact cancellation of emittance growth due to coupled transverse dynamics in solenoids and RF couplers," *Phys. Rev. Accel. Beams*, vol. 21, no. 1, Jan. 2018, Art. no. 010101.

[32] M. Maier *et al.*, "Complete transverse 4D beam characterization for ion beams at energies of few MeV/U," in *Proc. 28th Linear Accel. Conf. (LINAC)*, East Lansing, MI, USA, 2017, pp. 720–724.

[33] C. Xiao, O. K. Kester, L. Groening, H. Leibrock, M. Maier, and P. Rottländer, "Single-knob beam line for transverse emittance partitioning," *Phys. Rev. Special Topics-Accel. Beams*, vol. 16, no. 4, Apr. 2013, Art. no. 044201.

[34] H.-J. You, S.-W. Jang, Y.-H. Jung, T.-H. Lho, and S.-J. Lee, "Design and fabrication of a superconducting magnet for an 18 GHz electron cyclotron resonance ion/photon source NFRI-ECRIPS," *Rev. Sci. Instrum.*, vol. 83, no. 2, 2012, Art. no. 02A326.

[35] H. You, S. Jang, W. Choo, Y. Jung, T. Lho, and S. Yoo, "Development status of the 18 GHz superconducting electron cyclotron resonance ion source at National Fusion Research Institute," *Rev. Sci. Instrum.*, vol. 85, no. 2, 2014, Art. no. 02A916.

Garam Hahn received the Ph.D. degree in accelerator physics from the University of Seoul, Seoul, Republic of Korea, in 2017.

He was a Research Staff with Korea Institute of Radiological and Medical Sciences, Seoul, from 2008 to 2018. Since 2019, he has been a Senior Researcher with Pohang Accelerator Laboratory, Pohang University of Science and Technology (POSTECH), Pohang, Republic of Korea. His research interests include the development of beam instruments and electro-magnets for various particle accelerators.

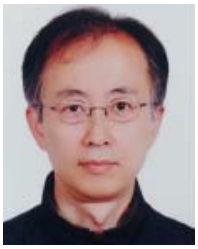

Tae-Keun Yang received the Ph.D. degree in nuclear physics from Pusan National University, Busan, Republic of Korea, in 1999.

He was a Post-Doctoral Research Fellow with Korea Institute of Geoscience and Mineral Resources, Daejeon, Republic of Korea, from 1999 to 2001. Since 2002, he has been a Principal Researcher with Korea Institute of Radiological and Medical Sciences, Seoul, Republic of Korea. His research interests include the development of beam instruments and medical devices.

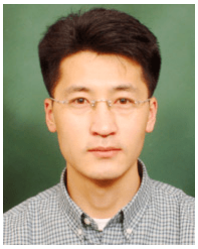

Hyun Jong You received the Ph.D. degree in plasma physics from Hanyang University, Seoul, Republic of Korea, in 2008.

He has been a Researcher with Korea Institute of Fusion Energy, Daejeon, South Korea, since 2008. He is currently working on the development of new microwave plasma and ion sources.

Ji-Gwang Hwang received the Ph.D. degree in accelerator physics from Kyungpook National University, Daegu, Republic of Korea, in 2014.

He was a Post-Doctoral Research Fellow with Korea Institute of Radiological and Medical Sciences, Seoul, Republic of Korea, from 2014 to 2015, where he was hired as the Senior Scientist afterward. Since 2016, he has been a Senior Researcher with the Helmholtz-Zentrum Berlin für Materialien und Energie, Berlin, Germany. His research interests include instrumentations for charged-particle beams and analog and digital signal processing.